

# Determining the Role of Fe-Doping on Promoting the Thermochemical Energy Storage Performance of $(\text{Mn}_{1-x}\text{Fe}_x)_3\text{O}_4$ Spinel

Alfonso J. Carrillo,\* Lidia E. Chinchilla, Ana Iglesias-Juez,\* Santiago Gutiérrez-Rubio, Daniel Sastre, Patricia Pizarro, Ana B. Hungría, and Juan M. Coronado\*


Mn oxides are promising materials for thermochemical heat store, but slow reoxidation of  $\text{Mn}_3\text{O}_4$  to  $\text{Mn}_2\text{O}_3$  limits efficiency. In contrast,  $(\text{Mn}_{1-x}\text{Fe}_x)_3\text{O}_4$  oxides show an enhanced transformation rate, but fundamental understanding of the role played by Fe cations is lacking. Here, nanoscale characterization of Fe-doped Mn oxides is performed to elucidate how Fe incorporation influences solid-state transformations. X-ray diffraction reveals the presence of two distinct spinel phases, cubic jacobite and tetragonal hausmannite for samples with more than 10% of Fe. Chemical mapping exposes wide variation of Fe content between grains, but an even distribution within crystallites. Due to the similarities of spinels structures, high-resolution scanning transmission electron microscopy cannot discriminate unambiguously between them, but Fe-enriched crystallites likely correspond to jacobite. In situ X-ray absorption spectroscopy confirms that increasing Fe content up to 20% boosts the reoxidation rate, leading to the transformation of  $\text{Mn}^{2+}$  in the spinel phase to  $\text{Mn}^{3+}$  in bixbyite. Extended X-ray absorption fine structure shows that Fe–O length is larger than Mn–O, but both electron energy loss spectroscopy and X-ray absorption near edge structure indicate that iron is always present as  $\text{Fe}^{3+}$  in octahedral sites. These structural modifications may facilitate ionic diffusion during bixbyite formation.

## 1. Introduction

First-row transition metal oxides present a huge technological relevance because they combine remarkable physicochemical properties with high abundance and low cost. In particular, Mn oxides are of interest in electrochemistry,<sup>[1,2]</sup> (photo) catalysis,<sup>[3–7]</sup> and for the development of batteries and magnetic devices.<sup>[8–10]</sup> The phase diagram of the Mn–O system shows several oxides with well-defined stoichiometry, ranging from  $\text{MnO}_2$  to  $\text{MnO}$ , which are stable in definite intervals of temperature and oxygen partial pressure.<sup>[11,12]</sup> This variety of structures and redox states is essential to explain the interest of these systems in multiple energy applications. For these technological uses, the capacity of control reversible redox transformations between the different phases is crucial and it has spawned the detailed research on the physicochemical properties of these materials using both experimental and theoretical perspectives.

A. J. Carrillo  
Instituto de Tecnología Química  
Universitat Politècnica de València – CSIC  
46022 Valencia, Spain  
E-mail: [alcardel@itq.upv.es](mailto:alcardel@itq.upv.es)

L. E. Chinchilla, A. B. Hungría  
Departamento de Ciencia de Materiales  
Ingeniería Metalúrgica y Química Inorgánica  
Universidad de Cádiz  
Campus Río San Pedro  
11510 Puerto Real, Spain

 The ORCID identification number(s) for the author(s) of this article can be found under <https://doi.org/10.1002/smt.202100550>.

© 2021 The Authors. Small Methods published by Wiley-VCH GmbH. This is an open access article under the terms of the Creative Commons Attribution-NonCommercial License, which permits use, distribution and reproduction in any medium, provided the original work is properly cited and is not used for commercial purposes.

DOI: [10.1002/smt.202100550](https://doi.org/10.1002/smt.202100550)

A. Iglesias-Juez, J. M. Coronado  
Instituto de Catálisis y Petroleoquímica  
CSIC  
28049 Madrid, Spain  
E-mail: [ana.iglesias@icp.csic.es](mailto:ana.iglesias@icp.csic.es); [jm.coronado@csic.es](mailto:jm.coronado@csic.es)  
S. Gutiérrez-Rubio, D. Sastre, P. Pizarro  
IMDEA Energy Institute  
28935 Madrid, Spain  
P. Pizarro  
Chemical and Environmental Engineering Group  
ES CET  
Universidad Rey Juan Carlos  
28933 Madrid, Spain

For applications at high temperatures, including chemical looping combustion,<sup>[13]</sup> solid oxide fuel cells,<sup>[14]</sup> catalysis,<sup>[15,16]</sup> thermochemical cycles for either hydrogen production<sup>[17,18]</sup> or heat storage,<sup>[19,20]</sup> bixbyite, Mn<sub>2</sub>O<sub>3</sub> and hausmannite, Mn<sub>3</sub>O<sub>4</sub>, phases are of special interest because they are stable in the temperature and pressure window under which these processes operate. Mn<sub>2</sub>O<sub>3</sub> presents a cubic structure (S.G. *Ia3*) with Mn<sup>3+</sup> placed in elongated octahedra, while Mn<sub>3</sub>O<sub>4</sub> is a tetragonal spinel (S.G. *I41/amd*), with Mn<sup>2+</sup> cations occupying the tetrahedral sites, and Mn<sup>3+</sup> cations placed on the octahedral ones. Reduction of Mn<sub>2</sub>O<sub>3</sub> occurs even at the high oxygen partial pressure of atmospheric air at temperatures above 700 °C. This transformation is reversible, although oxidation of Mn<sub>3</sub>O<sub>4</sub> to recover Mn<sub>2</sub>O<sub>3</sub> takes places at ≈200 °C lower, generating a significant thermal hysteresis loop and leading to a lower kinetic rate of the oxidation. This behavior limits the efficiency of these redox transformations and it has an impact on the performance of the thermochemical processes based on the Mn<sub>2</sub>O<sub>3</sub>/Mn<sub>3</sub>O<sub>4</sub> redox couple.

Chemical modifications of these oxides by doping with other transition metals, such Co, Cu, Cr, and Fe, or other abundant elements such Si have been explored as a way to enhance the redox behavior of the manganese oxides.<sup>[21–24]</sup> Beneficial effects in terms of increasing phase stability and heat storage capacity have been recently reported by Fe-doped CaMnO<sub>3</sub> perovskite.<sup>[25]</sup> Similarly, the incorporation of a significant amount of Fe (up to 20 mol%) into Mn<sub>2</sub>O<sub>3</sub> improves the energy storage density by almost 20% and narrows the hysteresis cycle, improving the exergy efficiency of the heat storage cyclic process.<sup>[26]</sup> This also leads to an increase in the oxidation rate, which follows a nucleation and growth mechanism, while preserving the stability of the systems.<sup>[27]</sup> Interestingly for practical considerations, these improvements of the redox behavior at high temperature are achieved by using an earth-abundant element and, accordingly, (Mn<sub>1-x</sub>Fe<sub>x</sub>)<sub>2</sub>O<sub>3</sub> materials are affordable for large-scale applications.

Introduction of Fe<sup>3+</sup> into the bixbyite lattice is facilitated by its size, which is identical to Mn<sup>3+</sup> in sixfold coordination, while differences in ionic radii between Mn<sup>2+</sup> and Fe<sup>2+</sup> are minimal. This leads to a wide range of stability for both (Mn<sub>1-x</sub>Fe<sub>x</sub>)<sub>2</sub>O<sub>3</sub> and (Mn<sub>1-x</sub>Fe<sub>x</sub>)<sub>3</sub>O<sub>4</sub> solid solutions, as it is shown in the corresponding phase diagrams.<sup>[28]</sup> Formation of an additional spinel phase with cubic symmetry (jacobsite, S.G. *Fd-3m*) has been observed after reduction of oxides with higher Fe-content. However, it is not clear to which extent (if at all) this additional phase is responsible of the improved properties of (Mn<sub>1-x</sub>Fe<sub>x</sub>)<sub>3</sub>O<sub>4</sub> oxides. Furthermore, Raman measurements suggest that a slight enlargement of the Mn–O bond is induced by Fe-doping, and this fact may enhance the readjustment of the lattice during the cationic diffusion involved in the oxidation of Mn<sup>2+</sup> cations.<sup>[27]</sup> X-ray absorption near edge structure (XANES) studies undertaken with Mn-doped ferrites, which have applications as catalysts and magnetic materials, have revealed a complex redox chemistry of these materials with mixed valence states and the affinity of Mn for octahedral sites.<sup>[29,30]</sup> In contrast, it has been reported that Fe<sup>3+</sup> is located in both tetrahedral and octahedral sites of the (Mn<sub>1-x</sub>Fe<sub>x</sub>)<sub>3</sub>O<sub>4</sub> spinels, but its distribution depends on iron content and even on preparation methods, which can lead to the formation of cation-deficient materials.<sup>[21,31]</sup> Accordingly, there is a need for additional

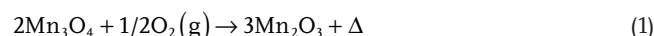
atomic-scale studies to unravel the ultimate role played by Fe in the spinel to bixbyite phase transformation.

With this aim, in the current study, a systematic investigation of selected (Mn<sub>1-x</sub>Fe<sub>x</sub>)<sub>3</sub>O<sub>4</sub> obtained by reduction at high temperature in air was carried out by using Rietveld refinements of the X-ray diffraction (XRD) data and using advanced electron microscopy techniques such as high-resolution scanning transmission electron microscopy (HRSTEM) with auxiliary spectroscopic techniques such X-ray energy dispersive spectrometry (XEDS) and electron energy loss spectroscopy (EELS). These analyses allow revealing the Fe distribution at atomic level in the spinels. Finally, the oxidation process of (Mn<sub>1-x</sub>Fe<sub>x</sub>)<sub>3</sub>O<sub>4</sub> to (Mn<sub>1-x</sub>Fe<sub>x</sub>)<sub>2</sub>O<sub>3</sub> was followed under in situ conditions by X-ray absorption spectroscopy (XAS) at both Mn and Fe K-edges, to monitor both structural modifications and variations of the oxidation state. Although in situ XRD results of these transformations were previously reported, this new approach using synchrotron radiation provides valuable information about the redox and structural transformations at local coordination spheres of both metals. All these insights are used to determine the influence of Fe on these high-temperature redox processes. A better understanding of the nanoscale dynamic of the dopants of these transition metal oxides might ultimately lead to designing more efficient materials for technologies that exploit the redox swing of these materials at high temperatures, such as thermochemical energy storage and chemical looping for processes such as methane combustion or reforming.

## 2. Results and Discussion

### 2.1. Effect of Fe Incorporation on the (Mn<sub>1-x</sub>Fe<sub>x</sub>)<sub>3</sub>O<sub>4</sub> Crystal Lattice

A series of iron-doped (1–20 mol% of Fe) manganese-based oxide materials in which the tetragonal hausmannite spinel phase is predominant, were prepared by Pechini method and subsequent high-temperature reduction, as reported elsewhere.<sup>[26,27]</sup> Our previous findings revealed that oxidation of the hausmannite phase (Equation (1)) is the slowest stage in the Mn<sub>2</sub>O<sub>3</sub>–Mn<sub>3</sub>O<sub>4</sub> reversible redox reaction, thus, the limiting step in the cyclic process



Fe-doping was shown to successfully raise the reoxidation reaction rate, in addition to provide other relevant improvements in the thermochemical heat storage characteristics. **Figure 1a** depicts a comparison of the conversion to bixbyite phase versus time for a (Mn<sub>1-x</sub>Fe<sub>x</sub>)<sub>3</sub>O<sub>4</sub> material with low Fe content ( $x = 0.01$ ) and a sample with higher Fe load ( $x = 0.2$ ), carried out in a thermobalance under air atmosphere and at 650 °C. **Figure 1a** shows that increasing the Fe content in (Mn<sub>1-x</sub>Fe<sub>x</sub>)<sub>3</sub>O<sub>4</sub> leads to faster oxidation reactions, as demonstrated in previous works.<sup>[26,27,32]</sup> Namely, the sample with  $x = 0.01$  needed 105 min to reach complete transformation to the oxidized phase, (Mn<sub>1-x</sub>Fe<sub>x</sub>)<sub>2</sub>O<sub>3</sub> bixbyite, whereas the sample with  $x = 0.2$  reached full conversion in 20 min, which represents a five-fold oxidation rate improvement. This fact confirms the positive influence of Fe incorporation in improving the Mn<sub>3</sub>O<sub>4</sub> oxidation

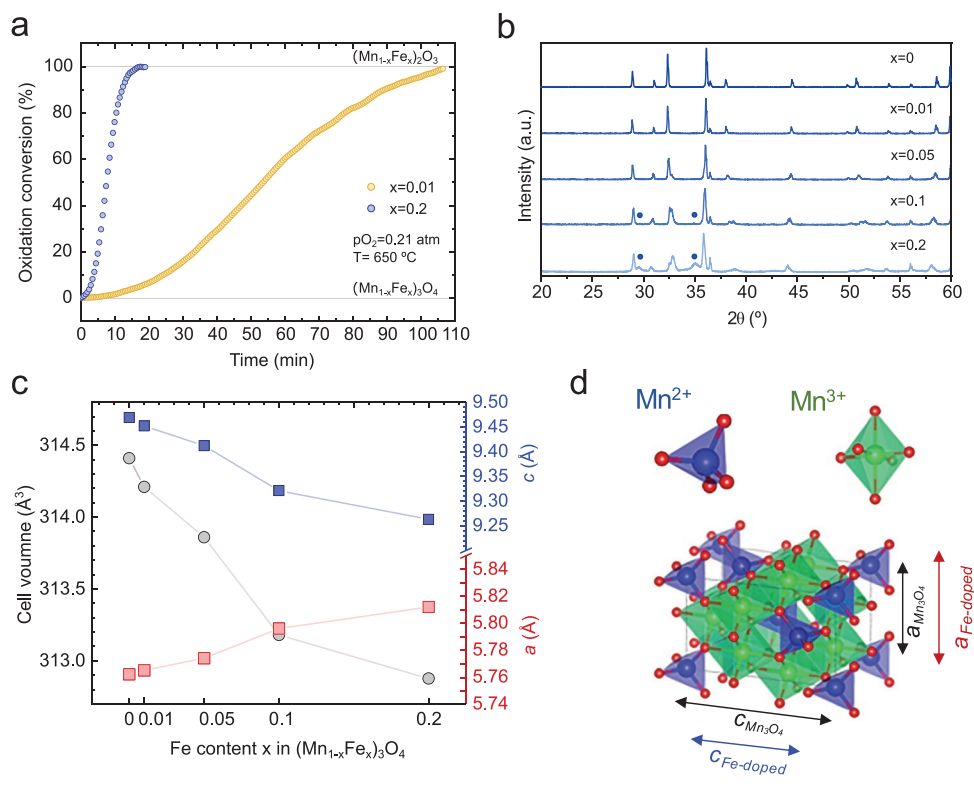


**Figure 1.** a) Oxidation conversion versus time for  $(\text{Mn}_{1-x}\text{Fe}_x)_3\text{O}_4$  materials with  $x = 0.01$  and  $0.2$ . Reaction was monitored thermogravimetrically at  $650 \text{ }^\circ\text{C}$  and using a constant air flow of  $50 \text{ mL min}^{-1}$ . b) X-ray diffractograms for  $(\text{Mn}_{1-x}\text{Fe}_x)_3\text{O}_4$  samples (\* denotes the reflections of jacobsite, cubic spinel, phase). c) Cell volume and tetragonal lattice parameters of the hausmannite phase present in  $(\text{Mn}_{1-x}\text{Fe}_x)_3\text{O}_4$  samples. d) Schematic of the  $\text{Mn}_3\text{O}_4$  tetragonal spinel phase depicting the tetrahedral-coordinated  $\text{Mn}^{2+}$  cations and the octahedral-coordinated  $\text{Mn}^{3+}$  cations.

kinetics. It should be noted that Figure 1a just depicts the two compositions of the Fe-doped Mn oxides series with the most divergent kinetics, to emphasize the positive effect of Fe-doping in progressively increasing the oxidation rate. In a previous work, we showed that the oxidation rate increased with doping degree up to  $x = 0.2$ . Then, we observed a slight rate decrease for  $x = 0.4$ , thus, the optimum Fe-doping content was established in  $x = 0.2$ .<sup>[26]</sup>

In order to shed light on the role of Fe cations in enhancing the oxidation rate, we first looked at the influence of Fe incorporation in the crystal structure of  $(\text{Mn}_{1-x}\text{Fe}_x)_3\text{O}_4$  oxides. Figure 1b shows the X-ray diffractograms of a series of  $(\text{Mn}_{1-x}\text{Fe}_x)_3\text{O}_4$  materials with  $x$  ranging from 0 to 0.2, which were reduced at  $1000 \text{ }^\circ\text{C}$  under air atmosphere in a tubular furnace, followed by cooling down to room temperature under inert Ar atmosphere to prevent reoxidation to the bixbyite phase. Figure 1b illustrates that all the samples present the characteristic reflections of the hausmannite tetragonal phase (ICDD: 00-024-0734). Sample with  $x = 0.2$  also exhibits the presence of cubic jacobsite phase (ICDD: 01-089-2808), which is also observed as traces in the oxide with  $x = 0.1$ . Additionally, the progressive replacement of Mn cations by Fe ones induces a shift in the reflections of the X-ray patterns. Careful analysis of the two most intense features shows that the peak located at  $2\theta = 32.4^\circ$ , which corresponds to the reflection  $[1\ 0\ 3]$  of  $\text{Mn}_3\text{O}_4$  is displaced to higher  $2\theta$  values with increasing the Fe incorporation. Contrarily, the most intense reflection  $[2\ 1\ 1]$  located at  $2\theta = 36.1^\circ$  shifts to lower  $2\theta$  values. Therefore, the former displacement of the peak indicates

a lattice contraction, whereas the latter feature points out to an expansion. These observations can be reconciled considering that upon Fe incorporation, one of the axes in the hausmannite is elongating whereas the other shrinking. To confirm this point, the cell volume and lattice parameters of each sample were determined by Rietveld refinement, Figure S1 in the Supporting Information. The refinement results illustrate that progressive replacement of Mn by Fe leads to an overall shrinkage of the tetragonal lattice, Figure 1c. Namely,  $\text{Mn}_3\text{O}_4$  sample ( $x = 0$ ) presents a cell volume of  $314.4 \text{ \AA}^3$ , decreasing down to  $312.9 \text{ \AA}^3$  for  $x = 0.2$ . Progressive reduction of Jahn–Teller effect in the  $\text{MO}_6$  octahedra by the gradual substitution of  $\text{Mn}^{3+}$  by  $\text{Fe}^{3+}$  can influence the variation in lattice parameter, despite both metal having identical ionic radii ( $0.645 \text{ \AA}$ ).<sup>[33]</sup> Interestingly, the cell volume values and Fe content ( $x$ ) exhibited a linear correlation for  $x = 0\text{--}0.1$ , which follows the Vegard's law indicating solid solution.<sup>[34]</sup> However, the oxide with  $x = 0.2$  lies above such trend since that material presents a considerable amount of jacobsite cubic spinel, which is most likely enriched in Fe as discussed below. Here, it should be noted that only the parameters of the tetragonal cell are depicted in Figure 1c. Quantification of the phase distribution inside  $x = 0.2$  sample indicates that 33.2% corresponds to the cubic spinel and the rest to the tetragonal phase. Considering this phase proportion and taking a linear extrapolation of the cell parameters plotted in Figure 1, it can be estimated that tetragonal hausmannite should correspond to an average of  $x = 0.13$ , and therefore cubic jacobsite should have an Fe-content around  $x = 0.34$ . Crystallite size for

each phase was determined by the Scherrer formula, revealing crystals of 38.9 and 8.7 nm for the hausmannite and jacobsite phases, respectively. These values are significantly smaller than those of the particles observed by STEM (see Section 2.2), suggesting the formation of polycrystalline aggregates.

As aforementioned, the observed peak shifts in Figure 1b also suggest that the crystal structure is experiencing an elongation with increasing Fe incorporation. The determined lattice parameters indicate that a minor enlargement is affecting the *a*-axis, whereas the *c*-axis is shrinking in a greater extent, which results in the overall cell volume decrease upon Fe incorporation. The *a*-axis value increases from 5.762 to 5.812 Å, whereas the *c*-axis shortens from 9.469 to 9.263 Å, for *x* = 0 and *x* = 0.2, respectively. As mentioned above, this lattice modification could be related to the decreasing influence of Jahn–Teller effect, resulting in more symmetric octahedra MO<sub>6</sub> by substituting Mn<sup>3+</sup> by Fe<sup>3+</sup>. Importantly, the *a*-axis elongation correlates well with our previous observations based on Raman spectroscopy, which suggest an increase in the M–O bond length for the *x* = 0.2 material.<sup>[27]</sup> Figure 1d shows a schematic depicting the dual shrinkage–elongation effect observed by XRD analyses, which reveals that Fe incorporation leads to crystal structures that slightly shift toward pseudo-cubic geometry. Namely, increasing the Fe content diminished the *c/a* values, e.g., *c/a* = 1.64 and 1.59 for *x* = 0 and *x* = 0.2, respectively.

## 2.2. Nanoscale Characterization of (Mn<sub>1-x</sub>Fe<sub>x</sub>)<sub>3</sub>O<sub>4</sub> Structures by HRSTEM

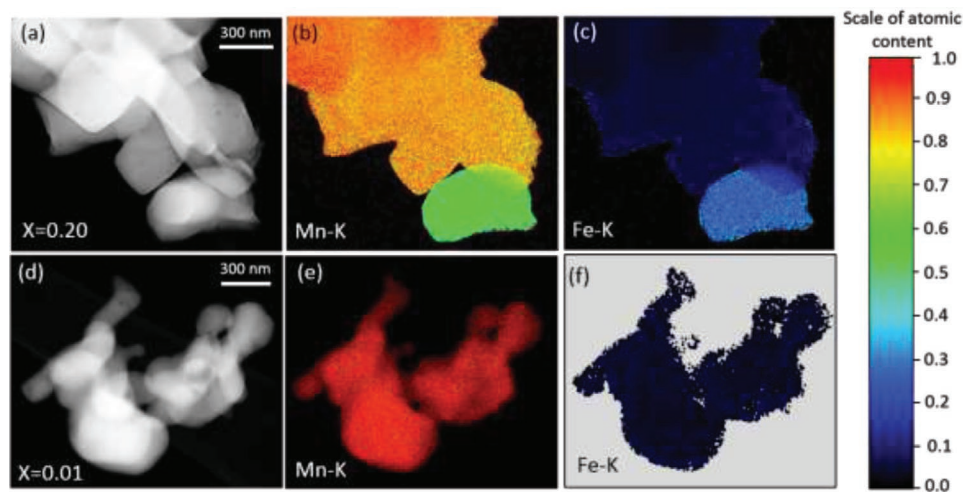
To elucidate the nanostructure of the crystal phases present in the (Mn<sub>0.8</sub>Fe<sub>0.2</sub>)<sub>3</sub>O<sub>4</sub> material, we performed a detailed microscopy exploration by means of high-resolution STEM, XEDS, and EELS techniques, and compared with a material with low Fe content exemplified by (Mn<sub>0.99</sub>Fe<sub>0.01</sub>)<sub>3</sub>O<sub>4</sub>.

Figure 2 shows two STEM-HAADF (high-angle annular dark-field) images and quantitative XEDS maps of representative areas of the (Mn<sub>0.8</sub>Fe<sub>0.2</sub>)<sub>3</sub>O<sub>4</sub> and (Mn<sub>0.99</sub>Fe<sub>0.01</sub>)<sub>3</sub>O<sub>4</sub> samples. In the case of the sample with the highest iron content,

(Mn<sub>0.8</sub>Fe<sub>0.2</sub>)<sub>3</sub>O<sub>4</sub>, the compositional analysis of the area displayed in Figure 2a shows that there is heterogeneity in the distribution of iron and manganese, with individual crystals being found with a higher concentration of iron than the nominal value. Thus, the crystal located at the bottom right in Figure 2a–c contains around 36 at% Fe, as compared to a concentration of ≈12 at% in the rest of the crystals in the area. That observation is consistent with the presence of a mixture of jacobsite and hausmannite crystal phases and their estimated compositions from XRD results, Figure 1b.

In order to further investigate the Fe-distribution in the (Mn<sub>0.8</sub>Fe<sub>0.2</sub>)<sub>3</sub>O<sub>4</sub> sample, a detailed statistical analysis was performed. Examination of this material at low magnification shows crystal aggregates containing particles in the range of 100–800 nm in size with variations in the Fe-content, Figure S2a,b in the Supporting Information. Compositional measurements by XEDS taken on 100 single particles, Figure S3 in the Supporting Information, again confirmed the heterogeneity of the composition of this sample at this scale. The atomic Mn and Fe contents are plotted in Figure S3c in the Supporting Information, revealing a material comprised by Mn-rich crystals ranging from 99 to 60 at%, with an average crystal composition of 78.3 at% Mn and 21.7 at% Fe, which is consistent with the targeted dopant content. According to the detailed analysis shown in Figure S3d in the Supporting Information, the highest fraction of crystals (34%) was found in the range of the nominal composition (80 ± 5 at%), while 29% exceeds the nominal percentage of Mn, with 7% consisting of crystals with up to 96 at% of this metal. On the other extreme of the composition, there are two more intervals below to the expected mean Mn content, from 60 to 65 and 66 to 75 at% Mn, representing 37% of the analyzed crystals.

According to the phase diagram of the Fe–Mn–O system,<sup>[35]</sup> at 1000 °C there is a wide range of composition, from Mn/(Fe+Mn) ratios of 1 to about 0.45, for the stability of spinel phases without the segregation of hematite, Fe<sub>2</sub>O<sub>3</sub>. In this composition interval, a mixture of jacobsite and hausmannite is expected for a Mn/(Fe+Mn) ratio between 0.7 and 0.95. Therefore, almost all the observed compositions for the (Mn<sub>0.8</sub>Fe<sub>0.2</sub>)<sub>3</sub>O<sub>4</sub> crystals are compatible with the co-existence



**Figure 2.** Representative STEM-HAADF images of (Mn<sub>1-x</sub>Fe<sub>x</sub>)<sub>3</sub>O<sub>4</sub> materials with a) *x* = 0.20 and d) *x* = 0.01. Sets of XEDS quantitative maps showing the spatial distribution of b,e) Mn–K and c,f) Fe–K from (a) and (b), respectively.



of the two spinel phases, hausmannite and jacobsite, also in accordance with the XRD results. However, it is expected that for particles with Fe higher than about 30 at% the predominant phase will be the cubic spinel. On the other hand, the relative wide distribution of Fe content between particles may be due to the low equilibration time during preparation of these oxides and it is consistent with the similarities of Mn and Fe cations and the wide range of stability  $(\text{Mn}_{1-x}\text{Fe}_x)_3\text{O}_4$  spinels.<sup>[35]</sup>

In contrast, the sample with the lowest iron content,  $(\text{Mn}_{0.99}\text{Fe}_{0.01})_3\text{O}_4$ , presents, in the analyzed areas shown in Figure 2d and Figure S2c in the Supporting Information, a homogenous distribution of iron and manganese in all the crystals, as it can be seen in the quantitative XEDS maps displayed in Figure 2e,f. This fact matches well with the observation of a single spinel phase extracted from the XRD analysis.

Closer investigation of the chemical distribution within a single grain was carried out at increased magnification in both samples with high ( $x = 0.20$ ) and low ( $x = 0.01$ ) Fe-content. XEDS and EELS line scans performed from the center to the surface of different crystals revealed no important composition fluctuations along the crystal in both samples (Figure S4a–d, Supporting Information). Thus, this indicates the absence of

phase segregations within the whole crystal and its boundaries, and a homogenous composition, in contrast with the variations observed between different agglomerates. This is in contrast with the recently reported formation of a core–shell structure in the case of  $(\text{Mn}_{0.8}\text{Fe}_{0.2})_3\text{O}_4$ , which showed grains with an iron-depleted surface layer and an inner area with a composition close to  $\text{MnFe}_2\text{O}_4$  jacobsite.<sup>[36]</sup> These differences with the phase distribution of the materials investigated here can arise from variations in the preparation route, including the reduction step.

Chemical composition was also examined at atomic resolution. Figure 3 shows the detailed high-resolution analysis of the samples  $(\text{Mn}_{0.8}\text{Fe}_{0.2})_3\text{O}_4$  and  $(\text{Mn}_{0.99}\text{Fe}_{0.01})_3\text{O}_4$  in Figure 3a,e, respectively. The simultaneous acquisition of maps by XEDS and EELS shows that iron and manganese cations are randomly distributed occupying the cationic positions, i.e., there are no separate Fe and Mn domains. In addition, the formation of iron aggregates can be ruled out, as shown in Figure 3b,f. EELS spectra from different locations were extracted for analysis and comparison. Figure 3c shows the spectra recorded at three different points in the ADF image belonging to the sample  $(\text{Mn}_{0.8}\text{Fe}_{0.2})_3\text{O}_4$  (Figure 3b). The simultaneous presence

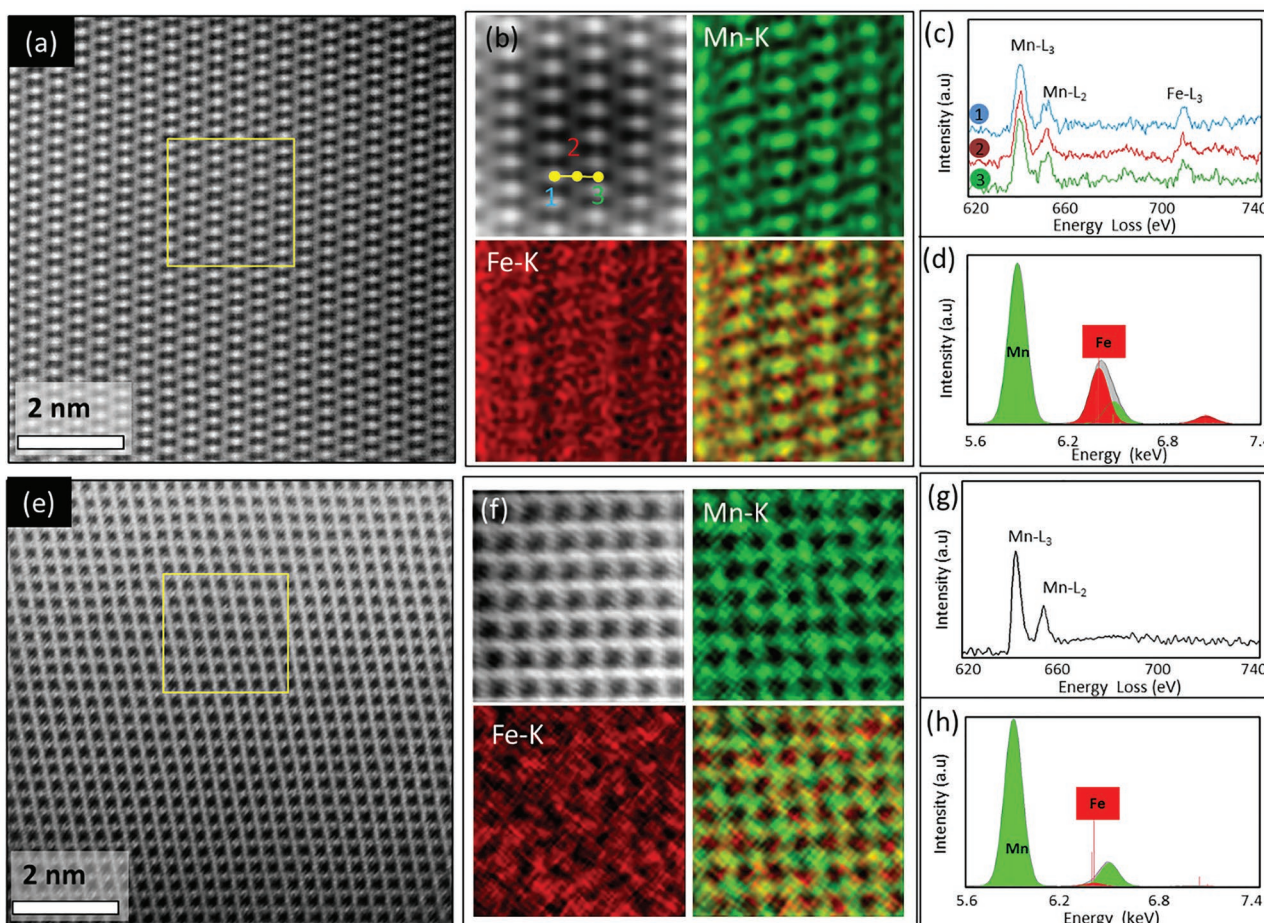


**Figure 3.** STEM-HAADF image and XEDS spectroscopy showing the atomically resolved crystal structures of: a,b)  $(\text{Mn}_{0.8}\text{Fe}_{0.2})_3\text{O}_4$  and e,f)  $(\text{Mn}_{0.99}\text{Fe}_{0.01})_3\text{O}_4$  materials. In the panels (b) and (f) are shown the set of XEDS elemental maps generated using Mn–K (green) and Fe–K (red) peaks and overlay Mn + Fe. c) Extracted EELS data (raw) from three different points in the ADF image in (b) and d) XEDS deconvoluted spectra from the whole ROI shown in (b). g) Extracted EELS data (raw) and h) XEDS deconvoluted spectra from the whole ROI shown in (f).

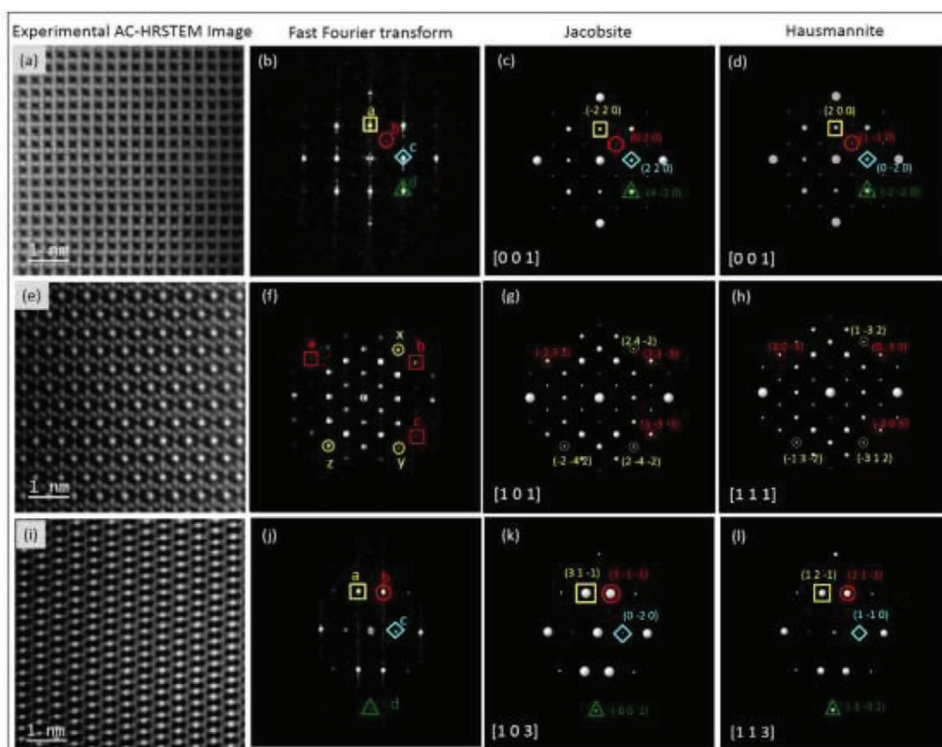


**Figure 4.** Experimental AC-HRSTEM-HAADF images of  $(\text{Mn}_{0.8}\text{Fe}_{0.2})_3\text{O}_4$  taken on crystals with various Fe content: a) 43 at%, e) 37 at%, and i) 28 at%. The corresponding digital diffraction patterns (DDPs) are included on (b), (f), and (j), respectively. Simulated dynamical electron diffraction patterns of  $(\text{Mn}_{0.8}\text{Fe}_{0.2})_3\text{O}_4$  jacobsite cubic phase along c) [001], g) [101], and k) [103] zone axis are compared to hausmannite tetragonal phase along d) [001], h) [111], and l) [113] zones axis, respectively.

of iron and manganese can be observed in all of them, regardless of their position. However, in the case of the sample  $(\text{Mn}_{0.99}\text{Fe}_{0.01})_3\text{O}_4$ , it is not possible to identify the iron presence at any position in the analyzed area, due to the low content of this element. Equally, in the EELS spectrum of the entire area under analysis (Figure 3g), only the manganese signal can be detected. Finally, Figure 3d,h depicts the deconvoluted XEDS spectra belonging to the whole area of images in Figure 3b,f, respectively, where the different amount of iron present in each of the samples can be certainly discerned.

Different HRSTEM images of both samples, with high and low Fe content, were analyzed to determine whether their crystallographic phase is hausmannite or jacobsite. These phases are exceedingly difficult to distinguish in most zone axes as they have very similar lattice parameters and atomic positions in the cationic sublattice. In the case of the sample with the highest iron content, three crystals with varying amounts of iron were chosen: 43, 37, and 28 at% and their HRSTEM images are shown in Figure 4a,e,i, respectively. The corresponding digital diffraction patterns (DDPs) are presented alongside each image, on which the interplanar spacing and angles can be measured. This information was used to determine the crystallographic phase orientation, by introducing atomic coordinates, lattice parameters, and spatial group in the Eje-Z program,<sup>[37]</sup> giving rise to this type of reflections. This was done by comparing the measured reflections in the DDP obtained from the experimental image with the dynamical diffraction patterns simulated for each of the phases. Table SI-1 of the Supporting

Information summarizes the values of interplanar spacing and angles measured in each of the DDP obtained from the experimental images shown in Figure 4 together with the values measured in the simulated DDP for hausmannite or jacobsite phases in the corresponding zone axes.

In the case of the DDP shown in Figure 4b, four reflections are analyzed, marked as “a,” “b,” “c,” and “d,” respectively. The experimental measurements of the spacing of these plane families are 98.5% close to the jacobsite and 95.6% close to the hausmannite. Since the measured spacing values in the zone axis [001] are so similar, these results are not conclusive. Also in both cases, the angles between the compared planes are identical and therefore it is challenging to discern the formation of the jacobsite phase in this crystal. Concerning the DDP shown in Figure 4f, the angles of families of planes that presented greater differences between jacobsite and hausmannite, marked as “a,” “b,” “c,” “x,” “y,” and “z,” have been contrasted to compare with the measurements of the angles in the experimental image, finding a similarity of 99.5% with jacobsite and 96.6% with hausmannite, as it is shown in Table SI-1 in the Supporting Information. Finally, regarding the analysis of the digital diffraction pattern shown in Figure 4j, the measurements of the distances indicated in the simulated dynamical diffraction patterns of the jacobsite phase in the zone axis [103] and hausmannite in [113] are so similar that it is challenging to discriminate between the two phases from these experimental measurements.

In view of these results, it seems that the crystals with a higher iron content appear to have a greater similarity with



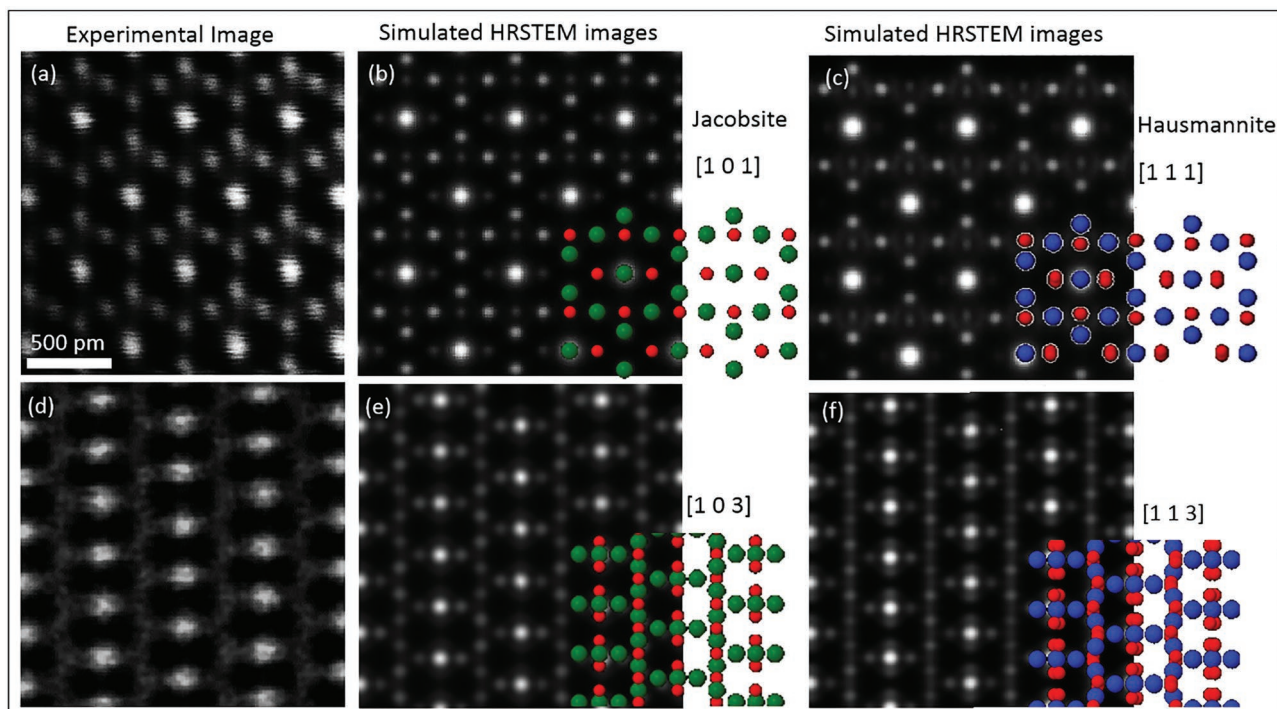


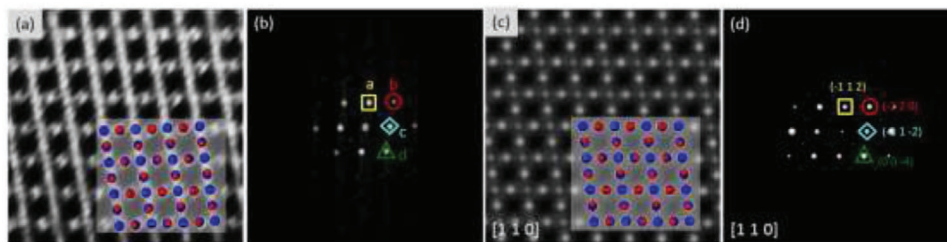
**Figure 5.** Experimental HRSTEM images of  $(\text{Mn}_{0.8}\text{Fe}_{0.2})_3\text{O}_4$  taken on crystals with various Fe content: a) 37 at%, and d) 28 at%. Simulated STEM images calculated for  $(\text{Mn}_{0.8}\text{Fe}_{0.2})_3\text{O}_4$  jacobsite cubic phase along b) [101] and e) [103] zone axis are compared to hausmannite tetragonal phase along c) [111] and f) [113] zones axis, respectively.

jacobsite, although the differences are so small that additional factors such as a small misalignment of the crystal with respect to the zone axis could affect the accuracy of the measurements and therefore the percentages of similarity cannot fully confirm the actual phases.

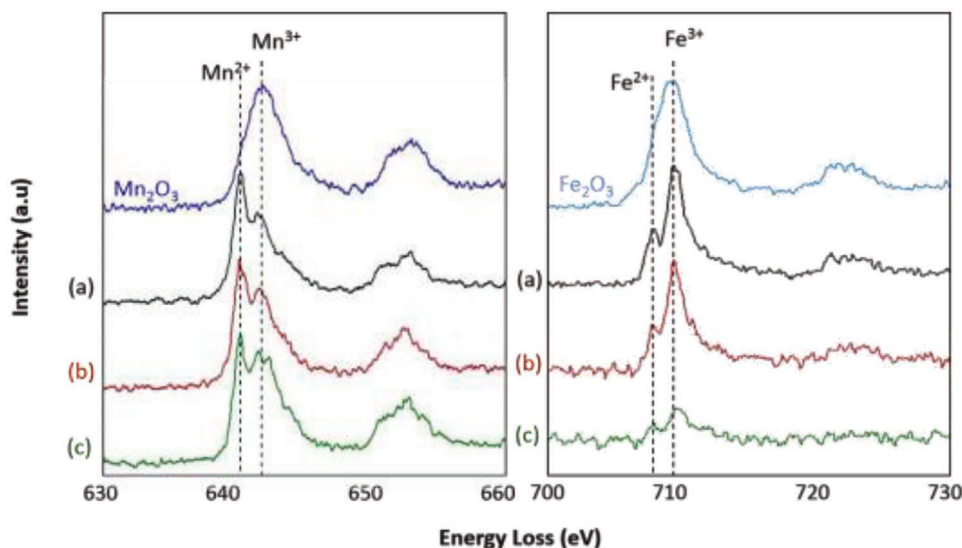
Taking into account the difficulty to discern both phases based on the analysis of the experimental and simulated digital diffraction diagrams, we proceeded to simulate the images of the jacobsite and hausmannite phases in the possible zone axes to try to reproduce the experimental images of the crystals with a lower iron content of sample  $(\text{Mn}_{0.8}\text{Fe}_{0.2})_3\text{O}_4$ . **Figure 5a** shows the experimental image and **Figure 5b** the simulated image considering a Jacobsite phase on the zone axis [101] and **Figure 5c** the simulated image of the hausmannite phase in zone [111]. The results of the image simulation of both phases in the shown zone axes do not show distinguishable differences between them, and in both cases, they are close to the experimental image. Similarly, to contrast with the experimental

image shown in **Figure 5d**, simulations of images of jacobsite-type crystals have been performed on the zone axis [103], **Figure 5e**, and hausmannite on the zone axis [113], **Figure 5f**. The most significant differences between hausmannite and jacobsite phase lie in a slight displacement of the oxygens in the anionic sublattice, with the cationic order being very similar in both phases, so that the Z-contrast images remain basically unchanged under these conditions.

The analysis of an experimental image of the sample with the lowest iron content  $(\text{Mn}_{0.99}\text{Fe}_{0.01})_3\text{O}_4$  shown in **Figure 6a** is much simpler, because when the interplanar spacings and angles measured in the digital diffraction pattern shown in **Figure 6b** are analyzed, they correspond unambiguously to the hausmannite phase on the zone axis [110]. The perfect coincidence with the image and the diffraction pattern simulated under these conditions can be seen in **Figure 6c,d**. Furthermore, analysis by electron microscopy allows determining the oxidation state of the elements present by means



**Figure 6.** a) Experimental HRSTEM images of  $(\text{Mn}_{0.99}\text{Fe}_{0.01})_3\text{O}_4$  and b) the corresponding fast Fourier Transform (FFT). c) Simulated STEM image calculated for  $(\text{Mn}_{0.99}\text{Fe}_{0.01})_3\text{O}_4$  – hausmannite tetragonal phase along [1 1 0] and d) the resultant dynamical electron diffraction pattern.



**Figure 7.** The ELNES of Mn and Fe  $L_{2,3}$  edges of  $(\text{Mn}_{0.8}\text{Fe}_{0.2})_3\text{O}_4$  taken on crystals with various Fe content: a) 40 at%, b) 35 at%, and c) 10 at% are compared to reference oxides  $\text{Mn}_2\text{O}_3$  and  $\text{Fe}_2\text{O}_3$ , respectively.

of EELS. **Figure 7** shows the energy-loss near-edge structure (ELNES) features in the  $L_{2,3}$  edges of Mn and Fe from a series of raw EELS spectra acquired in several crystals with different atomic content in iron (spectra corresponding to 40%, 35%, and 10% are displayed in **Figure 7**) belonging to sample  $(\text{Mn}_{0.8}\text{Fe}_{0.2})_3\text{O}_4$  compared to iron and manganese references. Analysis of the position of the  $L_3$  and  $L_2$  white lines of Mn, shown in **Figure 7** (left) for the crystals with a decreasing iron content, displays in all cases that the  $L_3$  lines (around 642 eV) are clearly comprised by two main peaks that can be attributed to the contribution of oxidation states 2+ and 3+. In fact, the shape of Mn- $L_2$  and  $L_3$  white lines from reference  $\alpha\text{-Mn}_2\text{O}_3$  appears as two peaks, without any clearly resolved multiple splitting as have been documented in the literature. Those results are consistent with several studies of manganese compounds with high oxidation state, in which Mn- $L_{2,3}$  edges can be used as a valence fingerprint, with  $L_3$  peak position shifted to higher energy as the formal valence is increased.<sup>[38,39]</sup> Additionally, the higher energy components of Mn- $L_3$  around 642 eV appear to slightly decrease with increasing dopant concentration, suggesting a higher proportion of  $\text{Mn}^{2+}/\text{Mn}^{3+}$  ratio for the crystallites with higher Fe content, as shown in **Figure S5** in the Supporting Information for a broad range of Fe content.

Regarding the ELNES for iron, **Figure 7** (right) shows the Fe  $L_{3,2}$ -edges in the crystals with different Fe content, demonstrating not significant differences among them, except for the peak intensity, which is proportional to the iron content. The ratio of the  $L_{3,2}$  excitation edges is normally used to determine the oxidation state, however, this approach cannot be used in the case of iron since coordination geometry strongly affects the Fe- $L_{3,2}$  ratios.<sup>[40]</sup> Besides, the energy position is also correlated with the oxidation state: the excitation edges shift to a higher energy-loss for a higher oxidation states. Thus, energy loss for  $\text{Fe}^{3+}$  is centered around 710.8 eV while 709 eV corresponds to  $\text{Fe}^{2+}$ .<sup>[41]</sup> In this case, **Figure 7** shows iron  $L_{2,3}$  edges with a maximum at 710.5 eV and a pre-peak located at 708.9 eV. The shape

of the spectra resembles hematite edges for trivalent iron with a shoulder at 1.6 eV previous to the  $L_3$  line related to octahedral coordinated ferric iron.<sup>[42]</sup> In order to evaluate the possibility of a mixture between  $\text{Fe}^{2+}/\text{Fe}^{3+}$ , Hyperspy routine<sup>[43]</sup> has been employed to study a phase separation in the Spectrum-Image of maximum iron content. The results lead to the conclusion of primary trivalent ground state as is shown in **Figure S6** in the Supporting Information.

### 2.3. In Situ XAS Monitoring of the $(\text{Mn}_{1-x}\text{Fe}_x)_3\text{O}_4$ Oxidation Process

Next, we turn to the in situ XAS study of both Mn and Fe K-edges of the  $(\text{Mn}_{1-x}\text{Fe}_x)_3\text{O}_4$  samples to reveal the oxidation state and coordination environment of both cations and their evolution during the oxidation reaction (the limiting step in the cycling process). These experiments were carried out isothermally at 600 °C in air flow. This operational temperature was dictated by both the characteristics of the reaction chamber used and the slower kinetics under these conditions, which facilitated detailed monitoring of the solid-state oxidation reaction.

**Figure 8** shows the initial XANES spectra of the as-prepared  $(\text{Mn}_{1-x}\text{Fe}_x)_3\text{O}_4$  samples and bixbyite,  $\text{Mn}_2\text{O}_3$  used as a reference. In all cases, the edge position and spectrum shape are very close to that of the undoped  $\text{Mn}_3\text{O}_4$  (hausmannite) oxide, and it is indicative of a similar structure and average oxidation state of the Mn atoms (coexistence of  $\text{Mn}^{2+}$  and  $\text{Mn}^{3+}$  states) for all samples. A closer examination of the first derivative shows a slight shift of the absorption edge to lower energies with increasing Fe content. This implies that the average oxidation state for Mn atoms slightly decreases thus, the  $\text{Mn}^{2+}:\text{Mn}^{3+}$  ratio increases with Fe content. The spectra also display a weak peak in the pre-edge region around 6541 eV, which is assigned to  $1s \rightarrow 3d$  transitions. This characteristic feature is adequate to identify not only the redox state but also the symmetry of the Mn cations of these materials. The intensity of the pre-edge



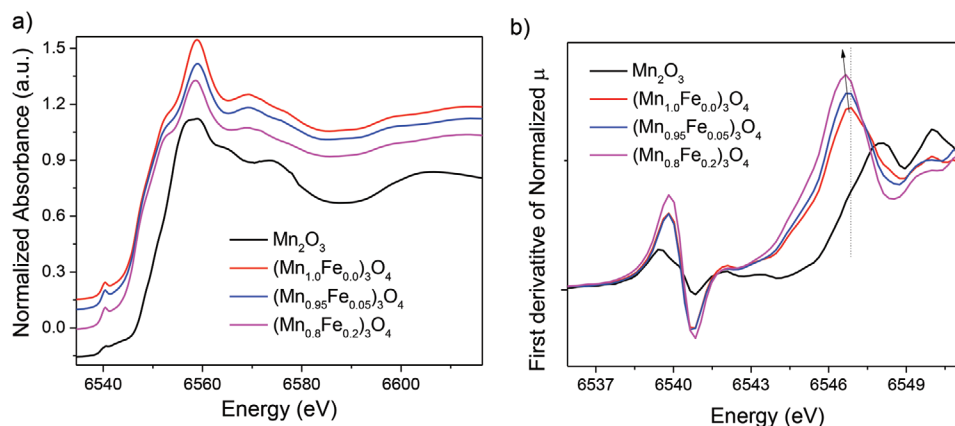


**Figure 8.** a) Initial normalized Mn K-edge XANES spectra at RT of  $(\text{Mn}_{1-x}\text{Fe}_x)_3\text{O}_4$  samples with  $x = 0.00, 0.05,$  and  $0.20$ , along with the  $\text{Mn}_2\text{O}_3$  reference. b) First derivative of the normalized XANES spectra.

increases for  $(\text{Mn}_{0.8}\text{Fe}_{0.2})_3\text{O}_4$  and shifts to higher energies (6542 eV), indicating that the proportion of Mn atoms located in octahedral sites decreases with regards to the unmodified hausmannite. Furthermore, the edge position of the Fe spectra of the reduced materials is located at 7122 eV, and this value provides evidence that iron atoms show a 3+ oxidation state in  $(\text{Mn}_{1-x}\text{Fe}_x)_3\text{O}_4$  samples (Figure S7, Supporting Information). Moreover, in the case of the sample with the highest Fe content, where two mixed oxide phases were detected, the average oxidation state is 3+ implying that all Fe is introduced as  $\text{Fe}^{3+}$  in both hausmannite and jacobite structures. Thus, these data confirm that  $\text{Fe}^{3+}$  atoms replace  $\text{Mn}^{3+}$  in octahedral centers of the  $(\text{Mn}_{1-x}\text{Fe}_x)_3\text{O}_4$  solid solution for the whole explored composition range.

Figure 9a–c displays the time evolution of the Mn K-edge for the mixed oxides containing 0%, 5%, and 20% of Fe when exposed to synthetic air under isothermal conditions at 600 °C. Pure  $\text{Mn}_3\text{O}_4$  spinel, without Fe, remains unchanged after 3.5 h of treatment due to the extremely slow oxidation kinetics of  $\text{Mn}_3\text{O}_4$  at such temperature. In the case of the sample with 5% of Fe, a slight shift to higher energies of the edge position over time can be appreciated. As there is a direct linear correlation between the Mn oxidation state and the edge position,<sup>[30,44,45]</sup> the displacement is indicative of a slow oxidation process. In addition, some variations in the extended X-ray absorption fine structure (EXAFS) signal became also apparent (see Figure S8, Supporting Information). These small changes reflect some modification of the Mn coordination environment, which are associated with the onset of the solid oxidation process, revealing a slow transformation of the doped oxide under these conditions. All these modifications are much more evident for the sample with the highest Fe content, 20%. Here, the Mn K edge gradually shifts to higher energies with reaction time, leading to a change of  $\approx 2$  eV. These modifications reflect the progressive oxidation of  $\text{Mn}^{2+}$  centers to  $\text{Mn}^{3+}$ , revealing a complete transformation to  $(\text{Mn}^{3+}_{1-x}\text{Fe}^{3+}_x)_2\text{O}_3$  in the case of the samples with 20% of Fe, while oxidation is only partial for the materials with 5% of Fe. Accordingly, the final XANES profile of the sample with 20% of Fe resembles that of cubic bixbyite  $\text{Mn}_2\text{O}_3$  phase. Correlatively, significant modifications in the EXAFS signal are observed as consequence of the

changes that take place in the Mn environment throughout the oxidation process. Moreover, the presence of isosbestic points in the XANES spectra (Figure 9a) indicates that the oxidation reaction involves two local environments in equilibrium. This can indicate the kinetically equivalent oxidation of the two spinels, which are structurally akin, to the bixbyite phase. Furthermore, there is a clear dependence of the oxidation rate with the Fe content: higher concentrations facilitate the quicker oxidation of Mn centers at isothermal conditions, consistently with previous reports.<sup>[26,32]</sup>

In parallel, measurements in the Fe K-edge were also carried out for the  $x = 0.2$  doped sample to examine iron behavior during the oxidation process in this material. As expected, the position of the absorption edge, initially corresponding to  $\text{Fe}^{3+}$ , did not change during the treatment. The shape of the pre-edge feature at 7112 eV confirmed the presence of  $\text{Fe}^{3+}$ . Only changes in the continue resonances were detected, ascribed to the modification of the local symmetry during the phase transition from the spinel to the bixbyite structure (see Figure S9, Supporting Information).

In order to gain further insights into the modifications of the chemical environment of the Mn sites during the oxidation, analysis of the EXAFS signal was performed. Due to the high-temperature reaction, EXAFS oscillations of the in situ acquired spectra for the samples are strongly damped with respect to those of the reference compounds acquired at room temperature (RT) (see Figure S10, Supporting Information). In addition, the coexistence of phases that have remarkably similar coordination distances, prevents from performing a detailed EXAFS analysis. Despite these limitations, the comparison of the EXAFS signals and their Fourier transforms (FT) recorded under the same experimental conditions on the three samples allows to extract valuable information regarding the first coordination shells.

The FT of the Mn  $k^2$ -weighted spectra are shown in Figure 9d–f. All  $(\text{Mn}_{1-x}\text{Fe}_x)_3\text{O}_4$  samples show a peak around 1.5 Å corresponding to the first Mn–O coordination shell. In the spinel structure, as mentioned above, Mn atoms are placed in both, tetrahedral and octahedral sites, so this observed feature in the FT-EXAFS must contain these two unresolved contributions. A second peak initially located around 2.5 Å is attributed to Mn–Mn

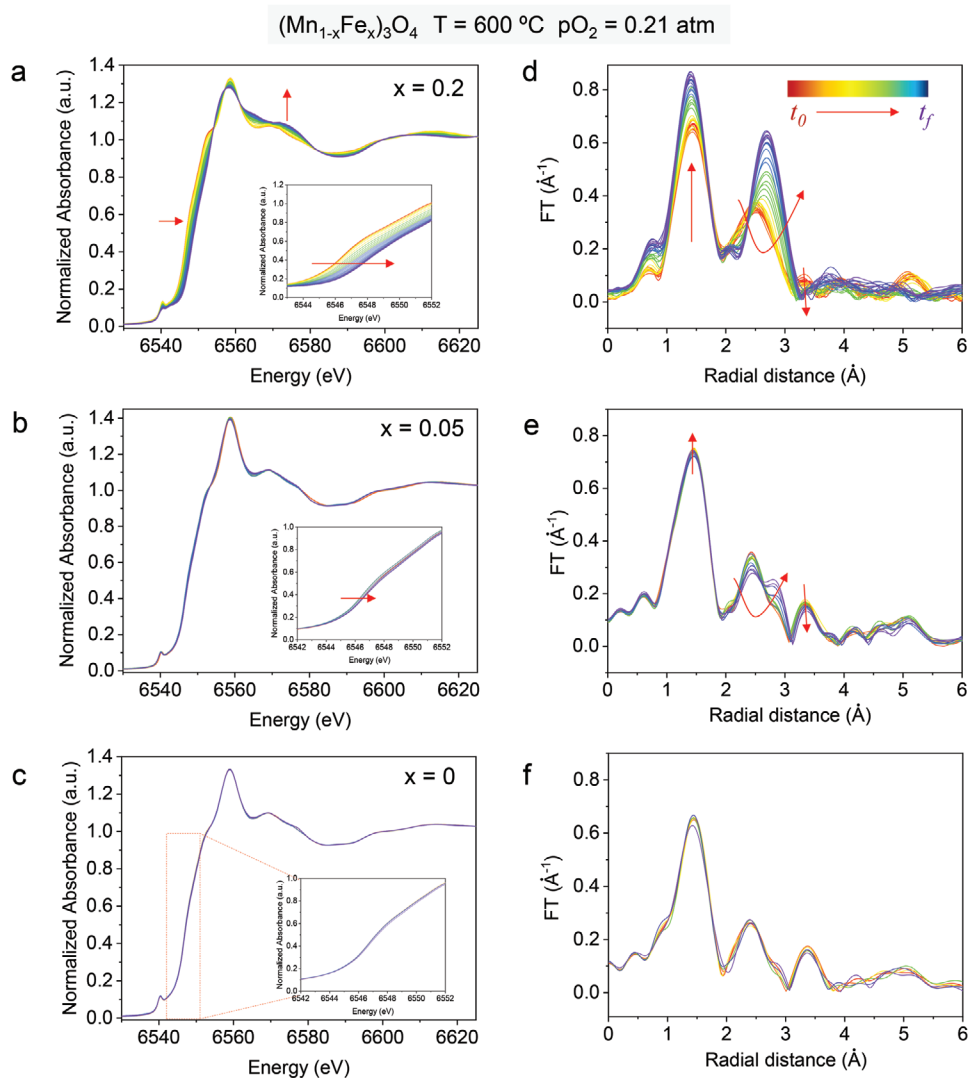


**Figure 9.** a–c) Time evolution of the Mn K-edge XANES spectra in air flow at 600 °C of  $(\text{Mn}_{1-x}\text{Fe}_x)_3\text{O}_4$  samples with a)  $x = 0.20$ , b)  $0.05$ , and c)  $0.00$ . Insets show a zoomed view of the edge region to stress the shift dependence on the Fe content. Spectra were acquired each 3 min, during 210 min. d–f)  $k^2$ -weighted Fourier transform of the Mn K-edge EXAFS signals ( $k$ -range from 2.9 to 11.5) during the isothermal treatment at 600 °C in air flow of  $(\text{Mn}_{1-x}\text{Fe}_x)_3\text{O}_4$  samples with d)  $x = 0.2$ , e)  $0.05$ , and f)  $0.0$ . Arrows mark the variation trend with time on stream under isothermal conditions.

distances between adjacent octahedral sites,  $\text{Mn}_{\text{Oh}}\text{--Mn}_{\text{Oh}}$ , while a third feature at  $\approx 3.4$  Å is assigned to the Mn–Mn distance among neighboring octahedral and tetrahedral sites,  $\text{Mn}_{\text{Oh}}\text{--Mn}_{\text{Td}}$ . For the material with no iron content, the FT profiles are similar along the isothermal treatment in air at 600 °C, in good relation to the absence of changes in the XANES spectra (Figure 9c). However, for the oxide containing 5 mol% of Fe, the treatment causes a gradual decrease of the second  $\text{Mn}_{\text{Oh}}\text{--Mn}_{\text{Oh}}$  coordination sphere and simultaneously a new feature at  $\approx 2.8$  Å slightly grows. Concurrently, the main contribution due to the Mn–O scattering path shows only a slight increase of intensity. These modifications can be interpreted as due to the initial distortion of the coordination polyhedron with the onset of the oxidation.

All these changes become more evident for the sample with the highest iron content (Figure 9d), as the Mn K-edge XANES

spectra anticipated (Figure 9a). For this sample, the intensity of the first peak grows up appreciably indicating an increase in the Mn–O coordination number with time in the air flow at 600 °C, which is fully consistent with an oxidative transformation. The contribution of the second coordination sphere progressively shifts to higher distances, increasing gradually and concomitantly to the decrease of the third coordination shell corresponding to  $\text{Mn}_{\text{Oh}}\text{--Mn}_{\text{Td}}$ . These changes reflect the transformation from the spinel, where Mn atoms adopt both tetrahedral,  $\text{MnO}_4$ , and octahedral,  $\text{MnO}_6$ , coordination to the bixbyite phase, where all Mn atoms occupy exclusively octahedral sites. In this respect, the enlargement of the overall  $\text{Mn}_{\text{Oh}}\text{--Mn}_{\text{Oh}}$  distance is also consistent with the reoxidation to  $(\text{Mn}_{1-x}\text{Fe}_x)_2\text{O}_3$ . On the other hand, the comparison between FT of the Fe K edge  $k^2$ -weighted EXAFS signals of the initial and final phases of the oxidation of  $(\text{Mn}_{0.8}\text{Fe}_{0.2})_3\text{O}_4$  sample

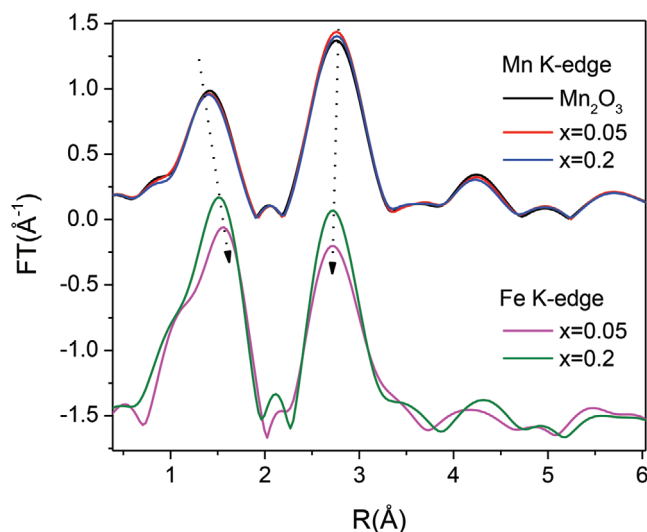


**Figure 10.** Fourier transforms of the Mn and Fe  $k^2$ -weighted spectra acquired ex situ at RT of  $\text{Mn}_2\text{O}_3$  and the  $(\text{Mn}_{1-x}\text{Fe}_x)_3\text{O}_4$  ( $x = 0, 0.05$ , and  $0.2$ ) samples after air treatment at  $600^\circ\text{C}$ .

(Figure S11, Supporting Information) indicates that there is almost no change in the local environment of the Fe; only a slight enlargement of the distance in the second coordination shell was observed, while the Fe–O contribution remains almost unchanged.

**Figure 10** shows the FT of the EXAFS signals corresponding to the two cationic environments, Mn and Fe, in the species for the  $(\text{Mn}_{1-x}\text{Fe}_x)_3\text{O}_4$  materials following the oxidation treatment, together with  $\text{Mn}_2\text{O}_3$ . Spectra were acquired at RT after ex situ treatment in air at high temperature. At both absorption edges, the pseudo-radial distribution profile is characteristic of the cubic bixbyite phase, with a first peak due to the oxygen sphere around the cation (either Fe or Mn) in octahedral coordination, M–O, and a second peak due to the cation–cation scattering path, M–M, in adjacent octahedral sites. However, clear differences in the local neighboring are visible depending on the central cation. In all the samples, regardless of the Fe content, the Mn centers present bond distances very similar to pure undoped  $\text{Mn}_2\text{O}_3$  phase. On the contrary, results of the Fe K-edge indicate that Fe–O bond length, which corresponds to  $\text{FeO}_6$  octahedra, increases with respect to Mn–O bond length, while the cationic network undergoes a variation around the Fe sites, which shows slightly smaller Fe–M distances than in the  $\text{Mn}_2\text{O}_3$  oxide.

Therefore, EXAFS data indicate that Fe-doping induces local distortions that may modify bond strengths and geometry of ion diffusion channels. In this line, although theoretical studies predict that Fe–O is larger than Mn–O for Fe-doped  $\text{Mn}_2\text{O}_3$ , an enlargement of Fe–O lengths is expected with increasing dopant content. Furthermore, these calculations revealed that the presence of oxygen vacancies in the vicinity of this metallic center may further increase the M–O bonds.<sup>[46]</sup> These structural modifications may enhance both the uptake and diffusion of oxygen and, the lattice readjustment during the cationic migration from tetrahedral to octahedral sites involved in the oxidation of  $\text{Mn}^{2+}$  cations.

### 3. Discussion

X-ray characterization of Fe-doped  $\text{Mn}_3\text{O}_4$  samples reveals a smooth linear variation of the cell parameters without any structural change for Fe concentration lower than 10%. In this range of compositions, the  $(\text{Fe,Mn})_3\text{O}_4$  materials show an ideal solid solution behavior, which is consistent with the size similarities of the two cations. On the other hand, for higher Fe concentration, the contribution of a second cubic spinel, jacobsite, becomes progressively important and, for a 20 mol% of Fe that phase constitutes about one third of the solid, as estimated by Rietveld analysis.

Although variations of unit cell parameters are not isotropic, showing opposite trends for *a*- and *c*-axis, the cell volume progressively decreases with increasing Fe content, and this suggests a slight overall shortening of cation–O distances. This observation could be consistent with the decrease of Jahn–Teller effect on substituting Mn by Fe, as it has been previously reported,<sup>[33]</sup> leading to a more symmetric  $\text{MO}_6$  octahedra. EXAFS analyses of the Mn K-edge were not able to ascertain this point because differences between octahedral and tetrahedral Mn–O cannot be resolved. In fact, these spectroscopic measurements do not detect any noticeable variations in Mn–O distances with Fe-doping. These results revise the previous suggestion of Mn–O enlargement in tetrahedral sites, as deduced from blue-shift of  $A_{1g}$  band of the Raman spectra with Fe-doping.<sup>[27,47]</sup> The overall view arising from the present study is a more nuanced transformation of the structure with Fe incorporation, where different coordination polyhedrals seem to experience different rearrangements. **Figure 11** shows a scheme that summarizes the structural transformation of  $\text{Mn}_3\text{O}_4$  with increasing Fe content as revealed in the present study.

Nanoscale analyses show a very uniform Fe distribution within each crystallite and no significant enrichment of any of the two metals on the surface or grain boundaries is detected, in contrast with some recent reports on  $(\text{Fe,Mn})_3\text{O}_4$ .<sup>[36]</sup> However, a rather wide variation of Fe content between grains of  $(\text{Fe,Mn})_3\text{O}_4$  is observed. This unexpectedly broad distribution of the dopant concentration within crystallites can be originated during the synthesis and it is likely to be facilitated by the size similarities between Fe and Mn cations. Nevertheless, Pechini method usually yields chemically homogenous materials, and this range of variation of the dopant distribution is probably eased here by the wide range of stability of  $(\text{Fe,Mn})_3\text{O}_4$  solid solution after high-temperature reduction and the short time of this synthesis stage.

In addition, it is also necessary to consider the influence on redox transformation of the formation of two spinels with different symmetries, which proportion is determined by the Fe content. Thus, as mentioned above, it can be roughly estimated assuming an ideal linear variation of cell parameters that in the sample with 20% Fe hausmannite phase should present an average Fe-content of  $x = 0.13$ , while jacobsite crystallites should correspond to approximately  $x = 0.34$ . HRSTEM analysis confirms the high crystallinity of these Fe and Mn spinels in the nanoscale and, although phase identification cannot be fully conclusive due to the close similarities between both tetragonal and cubic spinel structures, it seems very likely that grains with high Fe content correspond to jacobsite crystals.



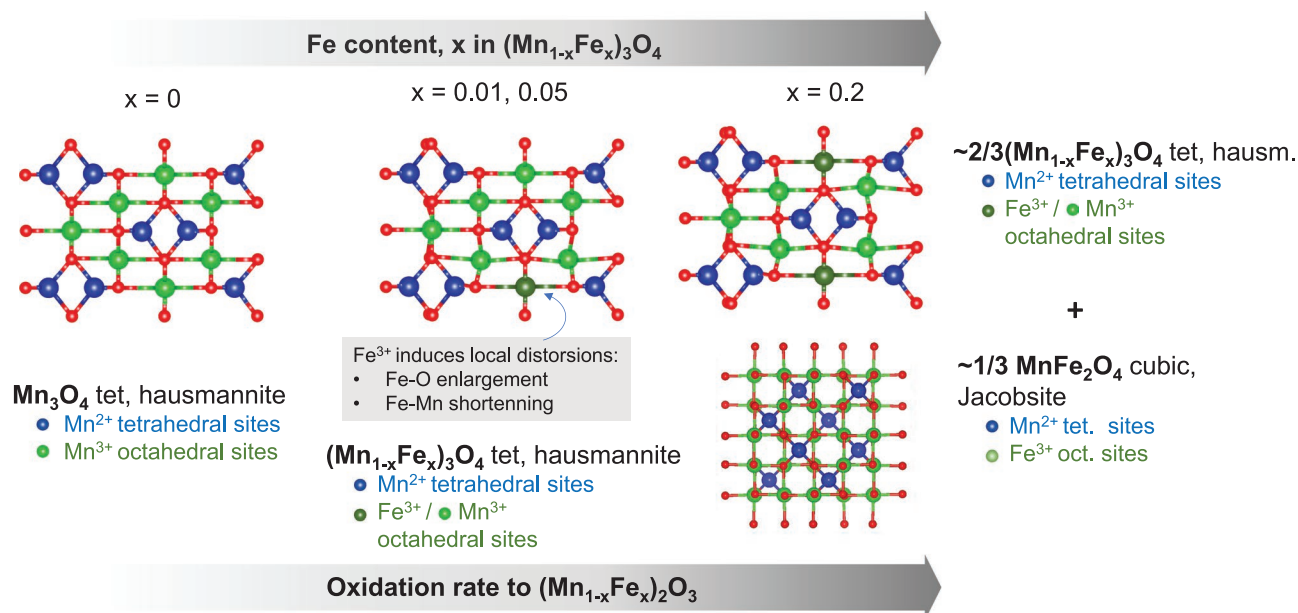


**Figure 11.** Schematic of the structural transformations of  $(\text{Mn}_{1-x}\text{Fe}_x)_3\text{O}_4$  with the variation of the Fe content.

EELS analysis at nanoscale reveals that Fe is present as  $\text{Fe}^{3+}$ . This is also confirmed by the Fe K-edge XANES data, which show a 3+ oxidation state for Fe atoms in the  $(\text{Mn}_{0.8}\text{Fe}_{0.2})_3\text{O}_4$  samples. Conversely, XANES and ELNES of Mn show both globally and at the nanoscale the presence of both  $\text{Mn}^{2+}$  and  $\text{Mn}^{3+}$  cations, which should correspond, respectively, to tetrahedral and octahedral sites of the normal spinel structure.<sup>[48]</sup> Careful analysis of these spectroscopic results suggests that the  $\text{Mn}^{2+}/\text{Mn}^{3+}$  ratio increases with Fe content, as expected due to the progressive incorporation of  $\text{Fe}^{3+}$  in octahedral sites (see Figure 11). This point is relevant because it circumscribes the redox interplay to the Mn sublattice, and settles a previous debate about the possible presence of  $\text{Fe}^{2+}$  species.<sup>[21]</sup> Therefore, apart from structural stability considerations, this fact establishes a maximum doping level, corresponding to the complete occupation of octahedral sites, before deterioration of the redox capacity of these materials occurs.

The XAS study, combining XANES and EXAFS, provides important insights into the variations of the local structure and oxidation state of Mn and Fe in these materials during the oxidation treatment at 600 °C. In situ XANES analysis of both Fe and Mn K edges of the sample containing 20% of Fe indicates that  $\text{Mn}^{2+}$  cations progressively oxidize to  $\text{Mn}^{3+}$  at 600 °C in air flow, while dopant remains as  $\text{Fe}^{3+}$  during this transformation. The material with 5% Fe content shows a much slower oxidation, while no changes are observed for the undoped sample under this mild temperature treatment. These results confirm the remarkable effect of Fe content on accelerating oxidation and corroborate that this dopant is not directly implied in the redox capacity of  $(\text{Mn}_{1-x}\text{Fe}_x)_3\text{O}_4$ . Furthermore, EXAFS shows that oxidation of the  $(\text{Mn}_{1-x}\text{Fe}_x)_3\text{O}_4$  materials implies a progressive increment of the oxygen coordination of the Mn centers, which is parallel to the oxidation of  $\text{Mn}^{2+}$  cations. Besides, these transformations involve the gradual rearrangement of the coordination polyhedral that results in the transformation

of tetrahedral positions into octahedral and a progressive increment of the of the  $\text{Mn}_{\text{Oh}}-\text{Mn}_{\text{Oh}}$  distances.

In the case of the sample with 5% of Fe, which according to the shift in the Mn K-edge is only partially oxidized, small changes observed in the EXAFS data also reflects the progressive modification of the Mn coordination environment associated with the onset of the oxidation of the solid, revealing a slow transformation to bixbyite under these conditions. Anyhow, modifications induced by Fe introduction in the solid, leading to larger Fe–O length and a slight shortening of the distance between Fe and adjacent cations compared to Mn local environment, affect both the oxygen bond strength and the geometry of diffusion paths and they can facilitate ion mobility during the readjustment of the structure for the transformation of spinel to bixbyite. Nevertheless, incorporation of oxygen into a solid is an apparently simple but intricate process that implies numerous events that can be ascribed to three main consecutive steps: surface reaction, bulk diffusion, and transference through grain boundaries.<sup>[49]</sup> All these stages may influence the kinetic of the process, and they should be considered in the present case to understand the overall role of Fe incorporation to the  $\text{Mn}_3\text{O}_4$ .

Although no specific study has been performed, Fe-doping does not seem to modify significantly grain dimension as neither transmission electron microscopy (TEM) nor XRD indicate any obvious trend in the variation in particle (with sizes in the 0.1–0.7  $\mu\text{m}$  range) or crystalline diameter with Fe incorporation. Neither significant modification of the Fe/Mn ratio is detected between bulk and the crystallites surfaces. So, the possible formation of  $\text{FeO}_x$  nanoclusters, which present high catalytic activity for certain oxidation reactions,<sup>[50]</sup> can be discarded in the present case as a relevant contribution to enhancement of the oxidation rate for  $(\text{Mn},\text{Fe})_3\text{O}_4$ . Nevertheless, surface  $\text{Fe}^{3+}$  cations, possibly as coordinatively unsaturated centers, may still play a significant role on  $\text{O}_2$  adsorption and activation. In

fact,  $(\text{Mn}_{1-x}\text{Fe}_x)_3\text{O}_4$  materials have proved to have a remarkable activity for the electrochemical oxygen reduction.<sup>[51]</sup> This can be related with the interplay of the two different adjacent metallic centers, which can facilitate the activation of the  $\text{O}_2$ . On the other hand, ionic diffusion may be facilitated by Fe-doping. Similar conclusion was drawn from the study of Li batteries where hausmannite structure has shown the existence of  $\text{Li}^+$  diffusion paths, and the kinetics of this process was found to be remarkably enhanced on the mixed Fe–Mn spinels with regards to undoped  $\text{Mn}_3\text{O}_4$ .<sup>[52]</sup> Moreover, significant increment of oxygen vacancies by Fe-doping of  $\text{Mn}_3\text{O}_4$  materials has been evidenced by Raman and X-ray photoelectron spectroscopy analyses.<sup>[16]</sup> In the same way, the enlargement of Fe–O distances observed here by EXAFS could also suggest the formation of those defects during oxidation of the solid. These vacancies could favor oxygen adsorption and transportation within the solid, and in this respect, recently reported density functional theory calculations confirm the positive effect of Fe-doping of both hausmannite and jacobsite on promoting  $\text{O}_2$  reduction to  $\text{O}^{2-}$ .<sup>[36]</sup> These theoretical results are consistent with the evidences of lattice rearrangement obtained here, that points out to a role of Fe incorporation, possibly with the participation of Mn sites in the vicinity, in promoting the reduction of  $\text{O}_2$  and enhancing diffusion paths within the  $(\text{Mn}_{1-x}\text{Fe}_x)_3\text{O}_4$  structure.

Theoretical results are consistent with the presence of the  $\text{Fe}^{3+}$  in octahedral sites on  $(\text{Mn}_{1-x}\text{Fe}_x)_3\text{O}_4$  spinels, as confirmed here by EELS at atomic level and more globally by XANES.<sup>[46]</sup> Equally, the higher formation enthalpy of Fe-doped bixbyite, as determined theoretically<sup>[46]</sup> provides the thermodynamic driving force for the oxidation of Fe-doped hausmannite. Moreover, formation of jacobsite is not detrimental for the reoxidation to bixbyite as evidenced by the favorable kinetic of the  $(\text{Mn}_{0.8}\text{Fe}_{0.2})_3\text{O}_4$  material. In fact, cubic spinels seem to present slightly lower but comparable activities than tetragonal phase. In this respect, the presence of isosbestic points in the in situ XANES of the  $(\text{Mn}_{0.8}\text{Fe}_{0.2})_3\text{O}_4$  material indicates a transformation to bixbyite from a single reduced state, despite the existence of a mixture of hausmannite and jacobsite. This is not surprising considering the already highlighted structural similarities between these two phases, although the less clearly defined isosbestic points in the Mn K-edge EXAFS signals suggest a transition between three phases. However, the variation of the relative proportion of spinels phases with the degree of doping is also relevant, because further increasing of Fe content up to 40% led to the solely presence of jacobsite, which results in slower oxidation kinetics. Therefore, it can be concluded that although jacobsite phase can efficiently participate in the redox cycle and being reoxidized to bixbyite, the higher transformation rate corresponds to the Fe-doped hausmannite phase, most likely due to its enhanced oxygen diffusion capacity. In addition, some synergy between the spinels on promoting oxidation can be also envisaged whether grains of these two phases come into contact. These observations highlight that the beneficial effect of Fe incorporation for oxidation kinetics and energy density should be adequately balanced with the possible lowering of the redox capacity at high concentration, to fully exploit the thermochemical properties of these mixed oxides.<sup>[26]</sup>

## 4. Conclusions

A set of Mn–Fe spinels with varying Fe content was synthesized and characterized at the nanoscale to shed light on the role of Fe on improving the oxidation kinetics. Detailed structural characterization at different scales was derived from XRD Rietveld analyses and further corroborated by EELS coupled with HRSTEM. Obtained results indicate that despite the homogenous distribution of Fe within the crystallite, without any relevant variation of the Fe/Mn ratio in surface, the content of this dopant varies broadly within grains for the samples with high Fe-content. This observation reflects the broad composition range for the stability of  $(\text{Mn}_{1-x}\text{Fe}_x)_3\text{O}_4$  spinels, with an ample region of coexistence of tetragonal and cubic phases. Although unambiguous identification of jacobsite and hausmannite at the nanoscale was not possible, it seems plausible that particles with high Fe content correspond to the cubic spinel. In situ isothermal XAS oxidation studies confirmed that increasing Fe content leads to faster oxidation rates as previously reported. This redox process implies only the Mn sublattice, as iron remains unchanged as  $\text{Fe}^{3+}$  during the process. The presence of isosbestic points in the XANES reveals nearly equal oxidation kinetic for both phases, remarking the similarities of hausmannite and jacobsite at the local environment of Mn sites. Therefore, the presence of the cubic jacobsite does not have any relevant kinetic effect for the studied range of doping. Comparative EXAFS analysis of the Mn and Fe K-edges indicates that increasing Fe-doping results in an important enlargement of Fe–O distances compared to Mn–O. This observation could be related with the formation of more open paths for ionic diffusion, and it provides relevant insight on the dynamic of the transformation to bixbyite. Without discarding a significant catalytic role of surface Fe sites, these structural modifications induced by the dopant can be a key aspect to promote the ionic mobility required for oxidation. This enhanced redox capacity of these Mn and Fe mixed oxides can be favorably exploited for different thermochemical energy-related technologies, such as chemical looping or thermal storage.

## 5. Experimental Section

**Materials Preparation:** Manganese–iron spinel samples  $(\text{Mn}_{1-x}\text{Fe}_x)_3\text{O}_4$ , with  $x$  ranging from 0 to 0.2, were synthesized by high-temperature reduction in air of the corresponding Fe-doped manganese sesquioxide,  $(\text{Mn}_{1-x}\text{Fe}_x)_2\text{O}_3$ , which were obtained by a modification of the Pechini method. In this procedure, as described elsewhere,<sup>[26,27]</sup> metal precursors, namely,  $\text{Mn}(\text{NO}_3)_2 \cdot 4\text{H}_2\text{O}$  (97%, Sigma-Aldrich) and  $\text{Fe}(\text{NO}_3)_3 \cdot 9\text{H}_2\text{O}$  (>98%, Sigma-Aldrich), were added to an aqueous solution of citric acid (CA,  $\geq 99.5\%$ , Scharlab) with a Me:CA molar ratio of 1:5, with constant stirring for 3 h at 70 °C. Afterward, ethylene glycol (EG,  $\geq 99.5\%$ , Sigma-Aldrich) was added with a molar ratio of CA:EG = 3:2 and kept during 2 h under stirring at 90 °C to form a gel, which was dried at 200 °C for 3 h and subsequently annealed at 450 °C for 4 h in air. Finally, the calcined gel was ground to fine powders and further calcined at 700 °C for 4 h under static air. In order to obtain solely the reduced phase, samples were heated up to 1050 °C ( $5\text{ °C min}^{-1}$ ), under an air flow of  $100\text{ mL min}^{-1}$ , and further cooled in Ar ( $100\text{ mL min}^{-1}$ ) atmosphere to avoid the samples reoxidation. The composition of the synthesized materials was obtained by inductively coupled plasma

optical emission spectrometry (ICP-OES) by using PerkinElmer Optima 3300 DV equipment, as described in a previous work.<sup>[36]</sup> The as-synthesized samples were digested in acid media by using an Anton Paar Multiwave 3000 microwave. The results of the ICP-OES elemental composition analyses are shown in Table S2 in the Supporting Information, for the as-synthesized  $(\text{Mn}_{1-x}\text{Fe}_x)_2\text{O}_3$  samples with  $x = 0.01\text{--}0.2$ . The values obtained with ICP-OES indicate that the targeted Fe-doping concentration is successfully obtained for all the samples.

**Materials Characterization—Crystal Phase Analysis:** Powder XRD analyses were carried out employing a Philips PW 3040/00 X'Pert MPD/MRD diffractometer using  $\text{CuK}\alpha$  radiation ( $\lambda = 1.54178 \text{ \AA}$ ) at a scanning rate of  $0.2^\circ \text{ s}^{-1}$ . Rietveld refinement was performed using the X'Pert HighScore Plus software.

**Materials Characterization—Oxidation Reaction Analysis:** Oxygen uptake was monitored by thermogravimetric analysis, TGA, a Netzsch STA 449 Jupiter F3 thermobalance was used for these studies. About 10 mg of Mn–Fe oxide,  $(\text{Mn}_{1-x}\text{Fe}_x)_2\text{O}_3$ , was placed in an alumina crucible and subjected to a reduction–oxidation cycle. Reduction was carried out at  $1000^\circ \text{C}$ , under a constant Ar flow of  $100 \text{ mL min}^{-1}$  to obtain the desired reduced phase  $(\text{Mn}_{1-x}\text{Fe}_x)_3\text{O}_4$ . Afterward, temperature was lowered to  $650^\circ \text{C}$  to perform the oxidation reaction under an air flow of  $100 \text{ mL min}^{-1}$ .

**Materials Characterization—High-Resolution Scanning Transmission Electron Microscopy:** The samples for electron microscopy studies were carefully grinded in a mortar into a very fine powder, and then deposited onto holey carbon-coated Cu grids. HRSTEM analyses were performed at 200 kV on a double aberration-corrected FEI Titan<sup>3</sup> Themis 60–300 microscope. The instrument was equipped with a monochromated, high brightness XFEG source; a high sensitivity Super-XEDS system, integrated by 4 window-less SDD detectors symmetrically arranged around the sample and the objective lens pole pieces; and a Gatan Quantum ERS image filter to perform ultra-high resolution EELS spectroscopy.

The acquisition of XEDS maps was carried out using a beam current of 50 pA, convergence angle of 19 mrad and 20 keV of range. Additionally, simultaneous EELS and XEDS measurements were carried out in spectrum image mode using a dispersion of 0.25 eV per channel, using a convergence angle of 18 mrad and collection semi-angle of 49 mrad, and acquisition time of 0.02 s in areas of about  $100 \times 100$  pixels.

In order to study electron ELNES of Mn and Fe, it employed a monochromated source at 80 kV, the spectrometer was set to 0.1 eV per channel for dispersion, dual-EELS mode, using a collection semi-angle of 12.5 mrad, and operated with relative low beam current ( $\approx 30 \text{ pA}$ ) to avoid damage radiation. Under those experimental conditions, a high energy resolution of 0.2 eV was obtained at the zero-loss peak (ZLP). All spectra were aligned according to ZLP and its dispersion was corrected. HRSTEM images were analyzed by measuring on the corresponding DDPs using Gatan's Digital Micrograph (DM) software. In addition, Eje-Z program<sup>[37]</sup> was used for the interpretation of HRSTEM images and modeling the possible  $(\text{Mn}_{1-x}\text{Fe}_x)_3\text{O}_4$  phases. HRSTEM image simulations were performed using TEM-SIM software.<sup>[53]</sup>

XEDS data were processed analyzing the Mn–K and Fe–K lines employing Cliff Lorimer method implemented in Bruker software and using Cu–K, O–K, and C–K lines for deconvolution of each spectrum.

EELS processing data, such as background and X-ray subtraction, were performed using Gatan's Digital Micrograph software. The elemental maps were generated using a power-law background removal model and signal extraction of the characteristic Fe– $L_{3,2}$  and Mn– $L_{3,2}$  edges. All spectra were calibrated and aligned with respect to the ZLP acquired simultaneously to the core loss region. Additionally, the spectra were analyzed in detail using  $\text{Fe}_2\text{O}_3$  and  $\text{Mn}_2\text{O}_3$  as reference materials applying a multivariate statistical post-treatment using Hyperspy program.<sup>[43]</sup> Using this methodology, it was possible to obtain relevant information on the oxidation states through the analysis of ELNES  $L_{2,3}$  of Fe and Mn.

**Materials Characterization—In Situ X-Ray Absorption Studies:** XAS experiments were performed at CLAES beamline at ALBA Synchrotron with the collaboration of ALBA staff. Pelletized samples,

$\approx 9 \text{ mg}$  of the redox oxide with BN as diluent, were placed in the solid gas multipurpose cell available at CLAES station for in situ measurements. After heating-up to the reaction temperature ( $600^\circ \text{C}$ ) in a He stream ( $20 \text{ mL min}^{-1}$ ), the gas composition was changed to synthetic air (20% v/v of  $\text{O}_2$  in  $\text{N}_2$ ) at a flow rate of  $20 \text{ mL min}^{-1}$ , and in situ Mn and Fe K-edge XAS spectra were collected in transmission mode using Si (311) crystal monochromator and ionization chambers for both  $I_0$  and  $I_1$ . A third ionization chamber was used to acquire the reference foil spectrum (Mn or Fe, respectively) simultaneously and ensure an appropriate energy calibration. An MS spectrometer was connected in the outlet to follow the reaction and check for leaks. Spectra normalization was performed with Athena program, part of Demeter package 0.9.26.<sup>[54]</sup>

## Supporting Information

Supporting Information is available from the Wiley Online Library or from the author.

## Acknowledgements

The authors thank the financial support from “Ramón Areces” Foundation (project SOLARKITE), Comunidad de Madrid and European Structural Funds (project ACES2030 P2018/EMT-4319), and University of Cádiz and European Structural Funds (project FEDER-UCA18-107139). A.J.C. thanks the financial support by Juan de la Cierva Formación Program (MICINN), grant FJCI-2017-33967. The authors acknowledge ALBA-CELLS Synchrotron facility for granting beamtime at CLAES (experiment 2016021666-2) and Electron Microscopy division located in the Servicios Centrales de Investigación Científica y Tecnológica (SC-ICYT) of the University of Cadiz. Assistance of Dr. Laura Simonelli during the XAS measurements in ALBA is fully appreciated.

## Conflict of Interest

The authors declare no conflict of interest.

## Author Contributions

A.J.C. synthesized the samples and performed the XRD characterization and contributed to the experimental design, conceptualization, and writing. L.E.C. and A.B.H. carried out the measurements, analyses, and the interpretation of the STEM results. S.G.R. and D.S. performed the XAS measurements, together with A.I.J., who analyzed these data and wrote the corresponding discussion. P.P. contributed to the experimental design and fund raising. J.M.C. conceived and designed the experiments, wrote the manuscript, and acquired funding for the research. All authors discussed the results and commented the manuscript.

## Data Availability Statement

Research data are not shared.

## Keywords

high-resolution STEM, in situ XAS, manganese oxides, redox, thermochemical heat storage

Received: May 25, 2021

Revised: August 12, 2021

Published online: September 9, 2021



- [1] S. Wang, C. Sun, N. Wang, Q. Zhang, *J. Mater. Chem. A* **2019**, *7*, 10138.
- [2] J. Liang, C. Jiang, W. Wu, *Nanoscale* **2019**, *11*, 7041.
- [3] T. Yoshinaga, M. Saruyama, A. Xiong, Y. Ham, Y. Kuang, R. Niishiro, S. Akiyama, M. Sakamoto, T. Hisatomi, K. Domen, T. Teranishi, *Nanoscale* **2018**, *10*, 10420.
- [4] M. Qiu, Z. Chen, Z. Yang, W. Li, Y. Tian, W. Zhang, Y. Xu, H. Cheng, *Catal. Sci. Technol.* **2018**, *8*, 2557.
- [5] J. Li, M. Zhang, E. A. Elimian, X. Lv, J. Chen, H. Jia, *Chem. Eng. J.* **2021**, *412*, 128560.
- [6] H. Xu, N. Yan, Z. Qu, W. Liu, J. Mei, W. Huang, S. Zhao, *Environ. Sci. Technol.* **2017**, *51*, 8879.
- [7] J. Kaczmarczyk, F. Zasada, J. Janas, P. Indyka, W. Piskorz, A. Kotarba, Z. Sojka, T. Stability, *ACS Catal.* **2016**, *6*, 1235.
- [8] L. Narayani, V. Jagadeesha Angadi, A. Sukhdev, M. Challa, S. Matteppanavar, P. R. Deepthi, P. Mohan Kumar, M. Pasha, *J. Magn. Magn. Mater.* **2019**, *476*, 268.
- [9] E. Thauer, X. Shi, S. Zhang, X. Chen, L. Deeg, R. Klingeler, K. Wenelska, E. Mijowska, *Energy* **2021**, *217*, 119399.
- [10] S. Li, X. Zhou, G. Fang, G. Xie, X. Liu, X. Lin, H. J. Qiu, *ACS Appl. Energy Mater.* **2020**, *3*, 7710.
- [11] A. J. Carrillo, J. Gonzalez-Aguilar, M. Romero, J. M. Coronado, *Chem. Rev.* **2019**, *119*, 4777.
- [12] S. Fritsch, A. Navrotsky, *J. Am. Ceram. Soc.* **1996**, *79*, 1761.
- [13] Q. Zafar, A. Abad, T. Mattisson, B. Gevert, M. Strand, *Chem. Eng. Sci.* **2007**, *62*, 6556.
- [14] Z. Yang, G. G. Xia, X. H. Li, J. W. Stevenson, *Int. J. Hydrogen Energy* **2007**, *32*, 3648.
- [15] W. Yang, S. Wang, K. Li, S. Liu, L. Gan, Y. Peng, J. Li, *Chem. Eng. J.* **2019**, *364*, 448.
- [16] L. Liu, J. Sun, J. Ding, Y. Zhang, T. Sun, J. Jia, *Inorg. Chem.* **2019**, *58*, 13241.
- [17] C. Brady, M. E. Davis, B. Xu, *Proc. Natl. Acad. Sci. USA* **2019**, *116*, 25001.
- [18] A. Bayón, V. A. De La Peña O'Shea, D. P. Serrano, J. M. Coronado, *J. CO<sub>2</sub> Util.* **2020**, *42*, 101264.
- [19] A. J. Carrillo, J. L. M. Rupp, J. M. Coronado, in *Energy Storage and Conversion Materials* (Ed: S. Skinner), The Royal Society of Chemistry, London **2020**, pp. 136–187.
- [20] A. J. Carrillo, D. P. Serrano, P. Pizarro, J. M. Coronado, *J. Mater. Chem. A* **2014**, *2*, 19435.
- [21] B. Gillot, M. Laarj, S. Kacim, *J. Mater. Chem.* **1997**, *7*, 827.
- [22] A. J. Carrillo, D. P. Serrano, P. Pizarro, J. M. Coronado, *J. Energy Storage* **2016**, *5*, 169.
- [23] A. J. Carrillo, P. Pizarro, J. M. Coronado, *J. Energy Storage* **2021**, *33*, 102028.
- [24] D. Bielsa, A. Zaki, P. L. Arias, A. Faik, *Sol. Energy* **2020**, *204*, 144.
- [25] E. Mastronardo, X. Qian, J. M. Coronado, S. M. Haile, *J. Mater. Chem. A* **2020**, *8*, 8503.
- [26] A. J. Carrillo, D. P. Serrano, P. Pizarro, J. M. Coronado, *ChemSusChem* **2015**, *8*, 1947.
- [27] A. J. Carrillo, D. P. Serrano, P. Pizarro, J. M. Coronado, *J. Phys. Chem. C* **2016**, *120*, 27800.
- [28] P. Franke, R. Dieckmann, *J. Phys. Chem. Solids* **1990**, *51*, 49.
- [29] F. H. Martins, F. G. Silva, F. L. O. Paula, A. G. Juliano De, R. Aquino, J. Mestnik-Filho, P. Bonville, F. Porcher, R. Perzynski, J. Depeyrot, *J. Phys. Chem. C* **2017**, *121*, 8982.
- [30] A. Campos, N. Lohitharn, A. Roy, E. Lotero, J. G. Goodwin, J. J. Spivey, *Appl. Catal., A* **2010**, *375*, 12.
- [31] B. Gillot, M. Laarj, S. Kacim, T. Battault, R. Legros, A. Rousset, *Solid State Ionics* **1996**, *83*, 215.
- [32] C. Agrafiotis, T. Block, M. Senholdt, S. Tescari, M. Roeb, C. Sattler, *Sol. Energy* **2017**, *149*, 227.
- [33] S. Lesturgez, G. Goglio, M. Duttine, A. Wattiaux, E. Durand, J. Hernandez, J. Majimel, A. Demourgues, *Chem. Mater.* **2016**, *28*, 4935.
- [34] L. Vegard, *Z. Phys.* **1921**, *5*, 17.
- [35] J. V. Crum, B. J. Riley, J. D. Vienna, *J. Am. Ceram. Soc.* **2009**, *92*, 2378.
- [36] D. Xiang, C. Gu, H. Xu, G. Xiao, *Small* **2021**, *17*, 2101524.
- [37] S. Bernal, F. J. Botana, J. J. Calvino, C. López, J. A. Pérez-Omil, J. M. Rodríguez-Izquierdo, *J. Chem. Soc., Faraday Trans.* **1996**, *92*, 2799.
- [38] L. A. J. Garvie, A. J. Craven, *Phys. Chem. Miner.* **1994**, *21*, 191.
- [39] H. Kurata, C. Colliex, *Phys. Rev. B* **1993**, *48*, 2102.
- [40] H. Tan, J. Verbeeck, A. Abakumov, G. Van Tendeloo, *Ultramicroscopy* **2012**, *116*, 24.
- [41] A. P. Brown, S. Hillier, R. M. D. Brydson, *J. Phys.: Conf. Ser.* **2017**, *902*, 012016.
- [42] S. Y. Chen, A. Gloter, A. Zobelli, L. Wang, C. H. Chen, C. Colliex, *Phys. Rev. B: Condens. Matter Mater. Phys.* **2009**, *79*, 104103.
- [43] F. de la Peña, T. Ostasevicius, V. T. Fauske, P. Burdet, E. Prestat, P. Jokubauskas, M. Nord, M. Sarahan, K. E. MacArthur, D. N. Johnstone, J. Taillon, J. Caron, V. Migunov, T. Furnival, A. Eljarrat, S. Mazzucco, T. Aarholt, M. Walls, T. Slater, F. Winkler, B. Martineau, G. Donval, R. McLeod, E. R. Hoglund, I. Alxneit, I. Hjorth, T. Henninen, L. F. Zagonel, A. Garmannslund, *5ht2, hyperspy/hyperspy: HyperSpy 1.3.1*, CERN, Genève, Switzerland **2018**.
- [44] H. Bertagnolli, *Ber. Bunsen-Ges. Phys. Chem.* **1989**, *93*, 229.
- [45] M. M. Najafpour, F. Ebrahimi, M. Amini, M. Rahimi, A. El-Sawy, S. L. Suib, *Dalton Trans.* **2015**, *44*, 15121.
- [46] E. Bazhenova, K. Honkala, *Catal. Today* **2017**, *285*, 104.
- [47] C. M. Julien, M. Massot, C. Poinignon, *Spectrochim. Acta, Part A* **2004**, *60*, 689.
- [48] K. E. Sickafus, J. M. Wills, N. W. Grimes, *J. Am. Ceram. Soc.* **1999**, *82*, 3279.
- [49] R. Merkle, J. Maier, *Angew. Chem., Int. Ed.* **2008**, *47*, 3874.
- [50] J. Qin, Y. Long, G. Gou, W. Wu, Y. Luo, X. Cao, S. Luo, K. Wang, J. Ma, *Catal. Sci. Technol.* **2020**, *10*, 5628.
- [51] H. Zhu, S. Zhang, Y. X. Huang, L. Wu, S. Sun, *Nano Lett.* **2013**, *13*, 2947.
- [52] X. Yu, C. Zhang, Z. Luo, T. Zhang, J. Liu, J. Li, Y. Zuo, J. J. Biendicho, J. Llorca, J. Arbiol, J. R. Morante, A. Cabot, *Nano Energy* **2019**, *66*, 104199.
- [53] E. J. Kirkland, *Advanced Computing in Electron Microscopy*, Springer, New York **2010**.
- [54] B. Ravel, M. Newville, *J. Synchrotron Radiat.* **2005**, *12*, 537.